Transparent and Stretchable Interactive Human Machine Interface Based on Patterned Graphene Heterostructures

*Sumin Lim, Donghee Son, Jaemin Kim, Young Bum Lee, Jun-Kyul Song, Suji Choi, Dong Jun Lee, Ji Hoon Kim, Minbaek Lee, Taeghwan Hyeon, and Dae-Hyeong Kim**

An interactive human-machine interface (iHMI) enables humans to control hardware and collect feedback information. In particular, wearable iHMI systems have attracted tremendous attention owing to their potential for use in personal mobile electronics and the Internet of Things. Although significant progress has been made in the development of iHMI systems, those based on rigid electronics have constraints in terms of wearability, comfortability, signal-to-noise ratio (SNR), and aesthetics. Herein the fabrication of a transparent and stretchable iHMI system composed of wearable mechanical sensors and stimulators is reported. The ultrathin and lightweight design of the system allows superior wearability and high SNR. The use of conductive/piezoelectric graphene heterostructures, which consist of poly(L-lactic acid), single-walled carbon nanotubes, and silver nanowires, results in high transparency, excellent performance, and low power consumption as well as mechanical deformability. The control of a robot arm for various motions and the feedback stimulation upon successful executions of commands are demonstrated using the wearable iHMI system.

1. Introduction

An interactive human-machine interface (iHMI) is a bidirectional electronic system that connects human and machines, allowing for the effective transfer of human intentions to the machine and the collection of feedback information from the machine. Wearable iHMI systems, in particular, have been in the spotlight with the recent development of wearable electronic devices, such as smart glasses[1] and smart watches.[2] Although wearable devices integrated with rigid sensors and actuators have shown the high performance and utility, there remain several limitations preventing their widespread use, such as the discomfort originated from the mechanical mismatch between the human body and bulky devices[3–5]; the unnatural appearance owing to the inflexibility of electronics[6]; and the signal artifacts that originate from the non-conformal attachment of the rigid sensors to the human body.[3–5] Therefore, novel ultrathin devices that can be conformally laminated onto human skin such that they have natural appearance, comfort, and high signal-to-noise ratio (SNR) are desired.

The adoption of flexible and stretchable designs and a concomitant reduction in the thickness and weight of devices are key goals with respect to the design of wearable electronics. Significant efforts have been made recently, including the development of stretchable inorganic electronics,[3,4,7] ultrathin and lightweight organic sensors,[8,9] flexible nanomaterial-based electronic skins,[10,11] self-powered motion sensors based on the triboelectric effect,[12,13] and highly sensitive flexible mechanical sensors.[14–17] Ultrathin and deformable designs allow for accurate data acquisition from the human body with minimum signal artifacts. However, these previously reported devices are made of opaque semiconductors and metals, which look different from human skin. In addition, many of these sensors lack power supply devices[3–5] and thus self-powering is important.

Transparent electronic nanomaterials can make wearable devices invisible, resulting in a natural look and improved aesthetics. For example, carbon-based nanomaterials (such as graphene (GP)[18] and carbon nanotubes[19] and metal nanowire (NW) networks (such as silver NWs[20] and gold NWs[21] have been intensively researched. These transparent nanomaterials

S. Lim, D. Son, J. Kim, Y. B. Lee, J.-K. Song, S. Choi, D. J. Lee, Prof. T. Hyeon and Prof. D.-H. Kim
Center for Nanoparticle Research
Institute for Basic Science (IBS)
Seoul 151–742, Republic of Korea
E-mail: dkim98@snu.ac.kr
S. Lim, Prof. T. Hyeon and Prof. D.-H. Kim
Interdisciplinary Program for Bioengineering
Seoul National University
Seoul 151–742, Republic of Korea
D. Son, J. Kim, Y. B. Lee, J.-K. Song, S. Choi, D. J. Lee, Prof. T. Hyeon, Prof. D.-H. Kim
School of Chemical and Biological Engineering
Institute of Chemical Processes
Seoul National University
Seoul 151–742, Republic of Korea
Prof. J. H. Kim
School of Mechanical Engineering
Pusan National University
Busan 609–735, Republic of Korea
Prof. M. Lee
Department of Physics
Inha University
Incheon 402–751, Republic of Korea

DOI: 10.1002/adfm.201402987

are also compatible with flexible electronics, as nanoscale structures result in a dramatic decrease of the flexural rigidity.[4,22] Meanwhile, self-powered mechanical sensors based on piezoelectric materials can decrease the power consumption of the electronic system.[23,24] A wide range of piezoelectric materials have been investigated, such as polymers including poly(vinylidene fluoride)[25,26] and polylactic acid (PLA),[27] and inorganic nanomaterials including zinc oxide[28] and lead zirconate titanate.[29]

We herein report a transparent and stretchable iHMI system composed of wearable sensors and stimulators that can monitor human motions, convert recorded data into signals for the machine control, deliver triggering signals to machines, and transfer feedback information from the machines to the human operator through electrotactile devices. The system is made of ultrathin and transparent nanomaterials, such as doped GP, single-walled carbon nanotubes (SWNTs), networks of silver NWs (AgNWs), and piezoelectric polymer (PLA), fabricated on transparent and deformable substrates (polymethylmethacrylate (PMMA, A2, MicroChem, USA), epoxy (SU8, MicroChem, USA), and polydimethylsiloxane (PDMS, Sylgard 184, Dow Corning, USA)). Given that the entire system is ultrathin and serpentine in designs,[30] it is stretchable and conformally integrated with human skin,[31] allowing for the collection of signals with minimal movement artifacts.[3] The high conductivity of GP/AgNW multilayers[32] enables the effective feedback for the electrotactile stimulation, which completes the closed-loop of the iHMI together with skin-conformable sensors. The iHMI system is used to demonstrate a robot control and transfer feedback signals to the operator.

2. Results and Discussion

Figure 1a shows images of the transparent and stretchable iHMI system, which consists of a piezoelectric motion sensor (top view) and an electrotactile stimulator (inset; bottom view). Partially detached images of the motion sensor (bottom left)

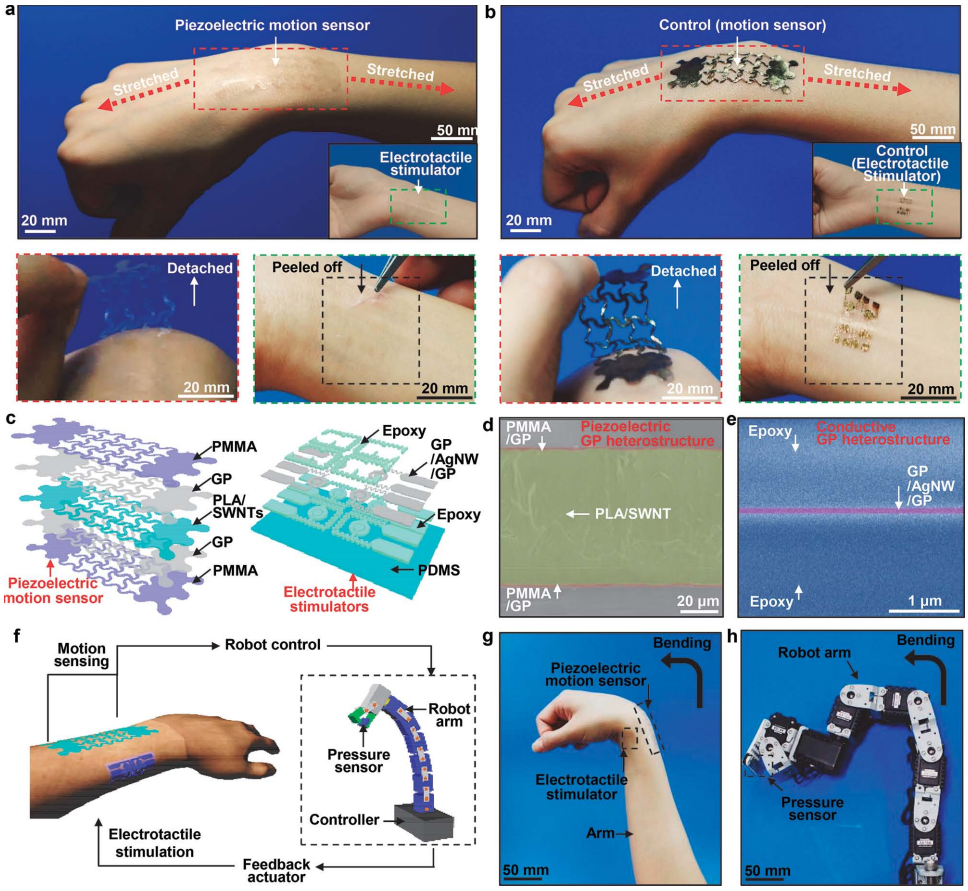

Figure 1. Transparent piezoelectric motion sensor and electrotactile stimulator for interactive human robot interface. a) Images of the transparent piezoelectric motion sensor (top) and the electrotactile stimulator (top, inset), in conformal contact with the top and bottom of a human wrist, respectively. Partially detached images of the motion sensor (bottom left) and the electrotactile stimulator (bottom right) are also shown. b) Images of the control specimens of the motion sensor and the stimulator, fabricated by replacing the GP electrodes with gold thin films. c) Exploded schematics of the patterned GP heterostructures used in the motion sensor (left) and the electrotactile stimulator (right). d) Colorized cross-sectional scanning electron microscopy (SEM) image of the patterned GP heterostructures used in the motion sensor (PMMA/GP: red, PLA: green). e) Colorized cross-sectional SEM image of the electrotactile stimulator (Epoxy: blue, GP/AgNW/GP: pink). f) Schematics of the closed-loop system of the iHMI, showing the flow of data corresponding to motion sensing and the resultant feedback stimulation. g) Representative image showing human motion to control the robot arm. h) Representative image of the corresponding position of the robot arm, which is controlled by the human motion.

and the electrotactile stimulator (bottom right) are also shown. The ultrathin, lightweight, and stretchable nature of devices enables the conformal integration with human skin, resulting in a high degree of comfort. The sprayed elastomeric film further enhances adhesion.[31] In addition, owing to their high transparency, devices remain very difficult to detect even after partial delamination. For the easy inspection of device designs, we fabricated control samples having the same design but made of gold instead of GP (Figure 1b). These skin devices have a natural and aesthetically pleasing appearance and ensure personal privacy.

Structural designs of devices and the material information are shown in the exploded illustration of patterned GP heterostructures (Figure 1c) that are used for the motion sensor (left) and electrotactile stimulator (right). The motion sensor consists of a piezoelectric GP heterostructure (Figure 1d), namely, piezoelectric polymer (PLA, ≈70 μm)/SWNT composite thin film sandwiched between GP electrodes and insulating layers. The GP is grown through a chemical vapor deposition process using copper[33] as the catalyst and is doped with gold salts. Layers of PMMA insulate devices. SWNTs improve the piezoelectric power-generation capability. The electrotactile stimulator is made of a conductive GP heterostructure (Figure 1e), namely, networks of AgNWs sandwiched between layers of doped GP, allowing for the better conductivity[32] and charge injection to the skin. AgNWs are synthesized in ethylene glycol using copper seeds and poly(vinylpyrrolidone) ligands (see the Supporting Information for the detailed synthesis of AgNWs). Figure 1d and e show cross-sectional scanning electron microscopy (SEM) images of piezoelectric and conductive GP heterostructures used for the motion sensor and the stimulator, respectively. The PMMA/GP and PLA layers of the motion sensor are shown in red and green, respectively, while the epoxy and GP/AgNW/GP layers of the stimulator are shown in blue and pink, respectively (see the Experimental Section and the Supporting Information for the detailed fabrication process).

A schematic illustration of the closed-loop iHMI system is in Figure 1f. The sensor monitors human motion and data collected are converted into signals to control the robot. The successful execution of commands by the robot generates feedback signals delivered to the device wearer through the electrotactile stimulator. For example, the process of grasping target objects by the robot is monitored by the piezoelectric pressure sensor integrated on the gripper. The successful completion of this task activates the electrotactile stimulator placed on the skin of the user. The conformal integration of stretchable piezoelectric sensors on human skin minimizes artifact signals and increases the accuracy of machine control. Figure 1g and h show representative images of the synchronized motion of a robot controlled by the human wearer (i.e., bending a robot arm by the commanding motion of the controlling human). Detailed demonstrations of the iHMI using this system are shown in Figure 6.

Transmittances of the stimulator, which is made of GP/AgNW/GP, and the motion sensor, which is made of PLA and PLA/SWNTs, are measured in the visible-light range (**Figure 2**a, 380–780 nm), and both devices exhibit high transparency. Optical images of the transparent devices and the control samples are shown in Figure S1 (Supporting Information). In its pristine state, GP has a higher sheet resistance than that of indium tin oxide (ITO) and thus has to be modified. Therefore, conductive GP heterostructures consisting of multilayers of GP doped with gold chloride and embedded AgNWs are used. Figure 2b shows the measured sheet resistances of the pristine (696.5 Ω/□), Au-doped (354.5 Ω/□), and AgNW-coated

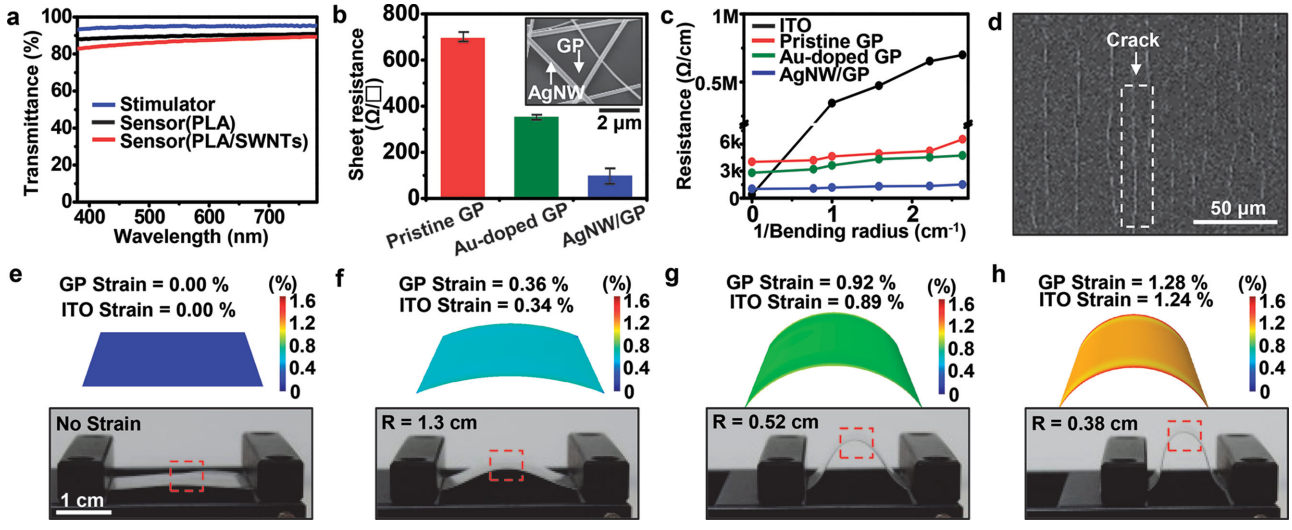

Figure 2. Optical, electrical, and mechanical characteristics of the fabricated GP heterostructure. a) Transmittances of the motion sensor (PLA: black, PLA/SWNTs: red) and electrotactile stimulator (blue) in the visible-light range. b) Sheet resistance of the pristine (red), Au-doped (green), and AgNW-coated (blue) GP heterostructures. The inset shows an SEM image of the AgNW-coated GP. c) Change in the resistance per unit length of the pristine, Au-doped, and AgNW-coated GP heterostructures, which varied with the reciprocal of the bending radius. d) SEM image showing the surface of the ITO film on the PET layer after the bending of the structure. The crack formed is indicated by a white arrow. e–h) FEA results showing the strain distribution of the GP heterostructure at different bending radii: e) $R = \infty$; f) $R = 1.3$ cm; g) $R = 0.52$ cm; h) $R = 1.3$ cm and corresponding images of the bent GP heterostructure.

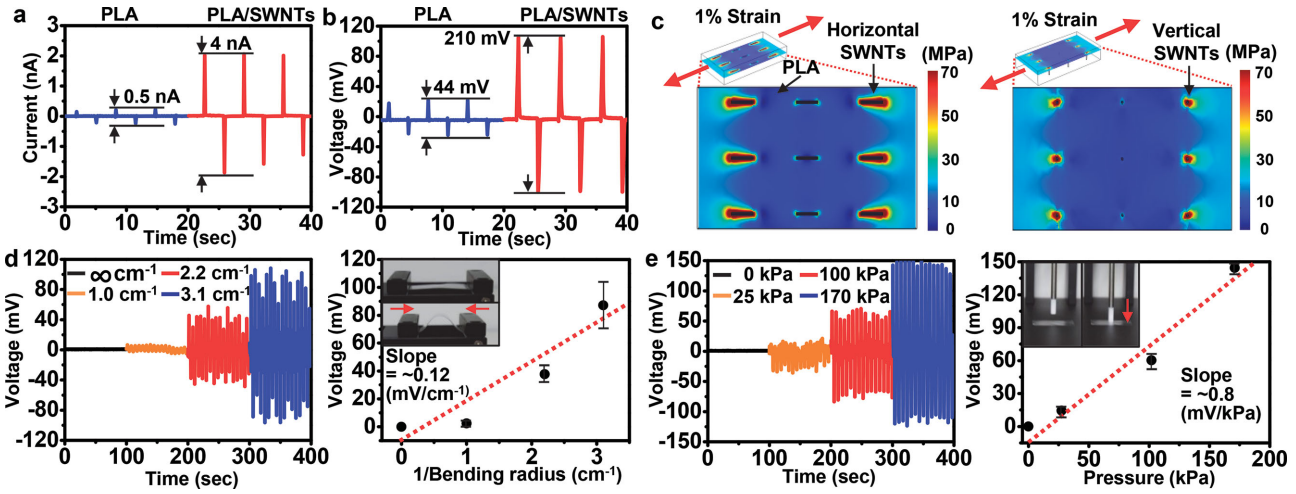

Figure 3. Electrical characteristics of the piezoelectric motion sensor. a) Output currents and b) voltages of the sensors with PLA (blue) and SWNT-embedded PLA (red) as a function of time. c) Strain distributions on the PLA film with horizontally (left) and vertically (right) aligned SWNTs, determined using FEA. d) The output voltage of the PLA/SWNT composite film versus time for different reciprocal of bending radii (left), and the corresponding output voltage as a function of the reciprocal of bending radius (right). The inset images show the bending of a film in the horizontal direction (red arrow). e) The output voltage of the PLA/SWNT composite film versus time at different pressures (left), and the corresponding output voltage as a function of the pressure (right). The inset images show the film being pressed in the vertical direction (red arrow).

(98.8 Ω/□) GP electrodes; the values indicate that the conductivity of GP can be successfully increased. The inset shows an SEM image of the AgNW-coated GP.

One advantage of the GP heterostructures with respect to ITO is their extremely high mechanical deformability. GP heterostructures and the ITO film are bent with different bending radii using a bending stage. The bending radii are determined on the basis of the pose of a bent human wrist (Figure S2, Supporting Information). The bending tests confirm that GP heterostructures maintain their high electrical conductivity even after being subjected to extreme bending, whereas the ITO film shows an abrupt increase of its resistance (Figure 2c). This increase of the resistance of the ITO film is caused by cracks formed during bending, as shown in an SEM image (Figure 2d). On the other hand, no crack is observed in GP heterostructures. Furthermore, the dramatic increase of the percent resistance change of the ITO film as a function of bending cycles shows that the ITO thin film is vulnerable to the bending-induced strain (Figure S3, Supporting Information).

Analyses based on theoretical mechanics corroborate these observations. Strain distributions of GP heterostructures and the ITO film for different bending radii are obtained by finite element analysis (FEA). Corresponding experiments are shown in Figure 2e–h. Red dotted boxes correspond to regions analyzed by FEA. FEA results indicate that local strain distributions of GP heterostructures and the ITO film for the same bending radii are not very different (see the Supporting Information for the details of FEA). However critical strains that cause mechanical fractures in the ITO film (< ≈1%)[34] and GP heterostructures (> ≈5%)[18] are different. The addition of the AgNWs network further enhances the mechanical robustness of GP heterostructures.[35] Therefore, conductive GP heterostructures can maintain their inherent electrical characteristics even during the dynamic motion of the human body.

Steps involved in integrating piezoelectric GP heterostructures are described in Figure S4 (Supporting Information). It is difficult to obtain high SNR from the pristine PLA, owing to the low amplitude of the generated piezoelectric voltage and current (blue plots in **Figure 3**a,b; see the Supporting Information for details of the measurement setup). To amplify generated piezoelectric signals, SWNTs are embedded in the PLA. The PLA/SWNT composite film shows a crystallinity of 32.4%, determined by X-ray diffraction analysis (Figure S5a, see the Supporting Information for details), as well as the high transparency (Figure 2a). The well-dispersed coexistence of PLA and SWNTs in the PLA/SWNT composite is confirmed by Raman spectroscopy (Figure S5b,c, Supporting Information). Under the same applied strain, the PLA/SWNT composite generates the current of ≈4 nA and the voltage of ≈210 mV (red plots in Figure 3a,b); these values are eight and five times higher than those in the case of the pristine PLA (blue plots in Figure 3a,b). The increases in the voltage and current are related to the SWNT concentration in the composite. The voltage and current generated by a film of a PLA composite containing SWNTs in half the original concentration (Figure S6a and b) are between the voltage and current of the pure PLA and the PLA/SWNTs with the original concentration (Figure 3a,b). This improvement in the piezoelectric property with the addition of SWNTs is maintained after multiple bending cycles (Figure S6c, see the Supporting Information for details). A piezoelectric voltage could also be generated by applying a shear stress (Figure S6d, Supporting Information).

Forward (Figure S6e, Supporting Information) and reverse (Figure S6f) connections switch the polarity, implying that such piezoelectric effect differentiates the direction of applied external force.[36] As a proof of concept, each polarity is observed when the bending direction is changed (Figure S6g, see the Supporting Information for the details of alignment of electric dipoles in a piezoelectric PLA film). When a PLA/SWNT

composite is subjected to the compressive or tensile strain, negative or positive charges accumulate adjacent to top and bottom electrodes. The accumulation of these charges is due to the strain-induced charge separation in PLA. Meanwhile, the high Young's modulus of SWNTs increases the local strain of PLA and thus maximizes the charge generation. This is evidenced by the fact that the strain concentrates near SWNTs, confirmed by FEA (1% strain is applied to the PLA/SWNT composite). Two different cases are modeled: SWNTs are either aligned horizontally or vertically in PLA (images on the left and right in Figure 3c, respectively). In both cases, the stress tends to concentrate near SWNTs.[37] To investigate the output voltage as a function of the applied strain, the generated voltage is measured at various bending radii, that is, d_{13} mode. Piezoelectric voltage output is known to be linearly proportional to the applied strain.[38] Figure 3d shows the corresponding voltage outputs (left) and the linear calibration curve, which has a slope of ≈0.12 mV/cm^{-1} (right). Figure 3e shows the piezoelectric voltage outputs in d_{33} mode generated by applying different pressures on the composite film (left); the linear correlation curve has a slope of ≈0.8 mV/kPa (right). Given that the relationship between the piezoelectricity and the externally applied mechanical stimuli is linear, the GP heterostructures are suitable for use as the sensing component in the iHMI.

To make a fully serpentine and stretchable design, the PLA/SWNT composite film is patterned using a mechanical punching process (Figure S7a). A custom-made punching mask is placed on the pressing machine, which is positioned on the film of piezoelectric GP heterostructures. The machine is then pressed with an appropriate pressure and released. The serpentine structure of the motion sensor allows it to be stretched (Figure S7b, Supporting Information). The sensor can also be placed conformally on the human skin such that it remains in close contact when the body is in motion (**Figure 4**a). It is true that the piezoelectric effect is less in patterned devices than non-patterned films. The efficient capture of human motions on the skin, however, requires the conformal integration of sensors onto the human body, which can be achieved by wavy designs. Therefore, the optimization of design is important to maximize both the conformal integration of devices to the skin and the high sensitivity of wearable piezoelectric sensors. Nevertheless, physical changes of the skin may cause changes in the interfacial adhesion of wearable devices, which result in signal output changes. This can be minimized by increasing the device stretchability and the interfacial adhesion force. The motion sensor does not generate an electrical potential when it is not deformed (upper left), while pressing (upper right), stretching (≈12% strain, lower left), or compressing (≈–31% strain, lower right) result in a voltage output. The amplitude and polarity of the generated potential depends on the degree and direction of the deformation, respectively. The generated potential is piezoelectric in nature; this is confirmed by the change in the voltage polarity in different connections (Figure S7c, Supporting Information). Strain distributions in the motion sensor, which induce the output signals (Figure 4a), are estimated through FEA (Figure 4b, see the Supporting Information for details); FEA results explain differences in amplitudes and polarities. By using four different motion-induced signals, four command signals to control the machine could be generated (Figure 6). Besides, more complex motion modes, such as the radial deviation, the ulnar deviation, the pronation and the supination, can be monitored by integrating multiple motion sensors in an array format.

After assigned commands are executed by the robot, feedback information can be transmitted to the human operator via an electrotactile stimulator, which forms a closed-loop of the iHMI. The electrotactile stimulator is also transparent and stretchable. The conformal integration with the human skin enables the effective charge injection. The schematic illustration of the fabrication process of the stimulator is in **Figure 5**a. The fabrication process starts with the deposition of a sacrificial layer (Cr/Ni, 7 nm/70 nm), on which the epoxy is patterned using photolithography. Then, GP/AgNW/GP multilayers are transferred onto the epoxy layer and then encapsulated with the additional epoxy layer. After the another patterning, the entire device is transfer-printed onto a PDMS/polyvinyl alcohol (PVA)

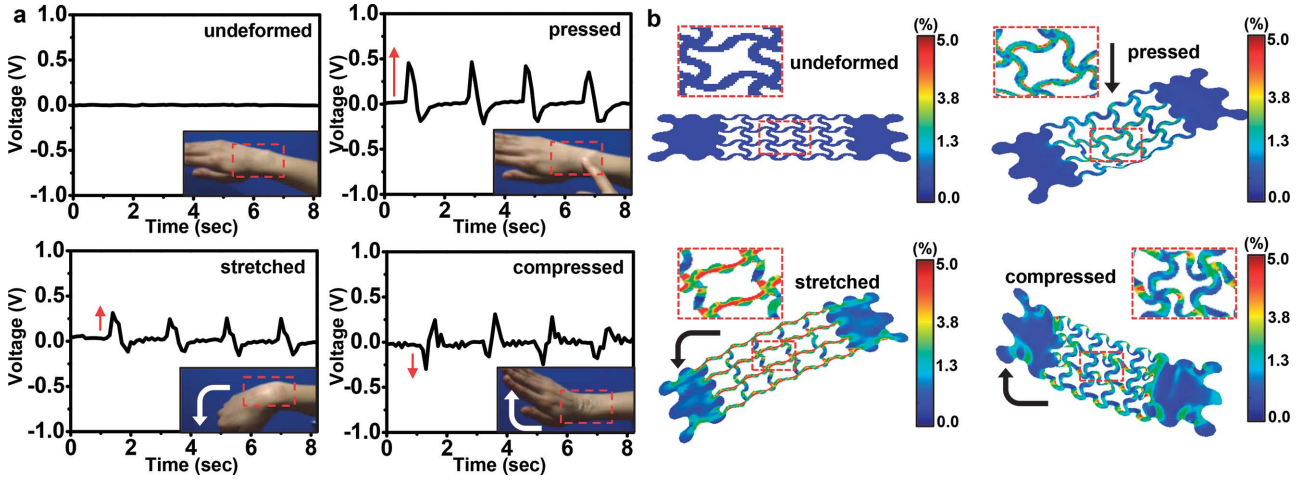

Figure 4. a) Plot of output voltage of the sensor in four modes (undeformed, pressed, stretched, and compressed) as a function of time, and images of the sensor in the four modes (bottom right inset of each graph). b) Strain distributions corresponding to the four modes (undeformed, pressed, stretched, and compressed), obtained through FEA.

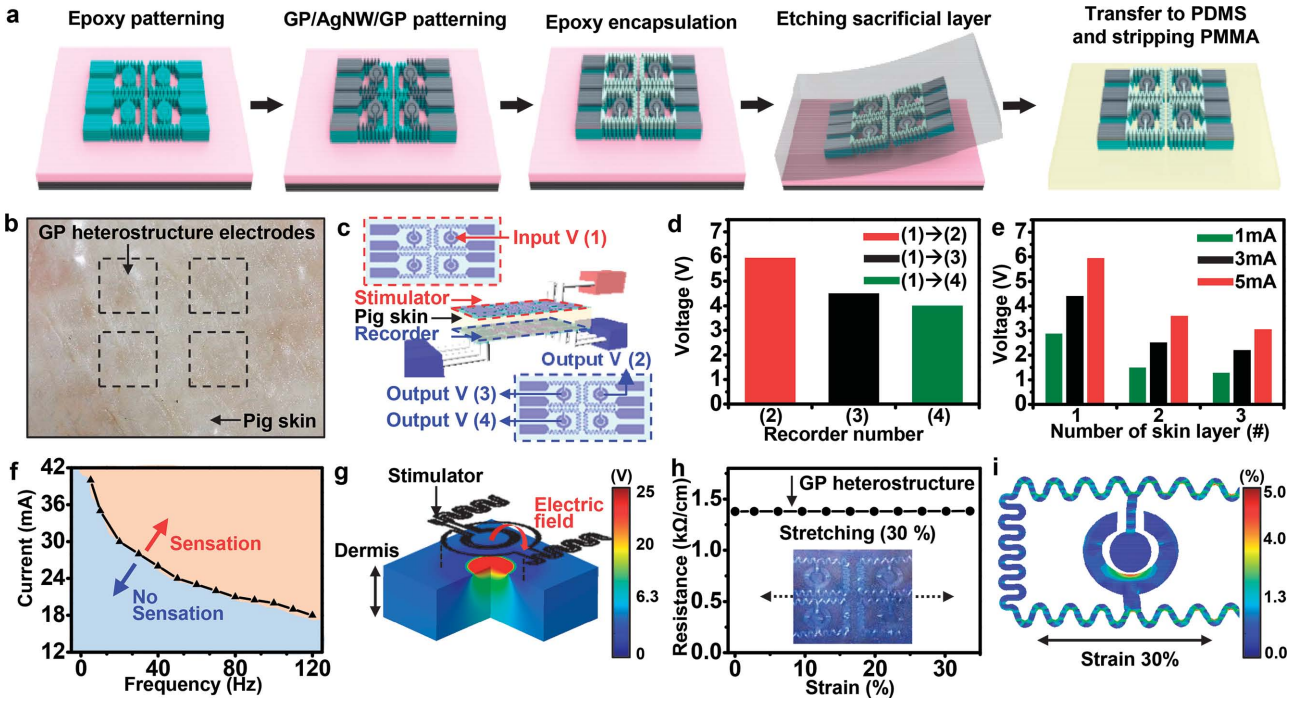

Figure 5. a) Schematic of the fabrication process of the transparent electrotactile stimulator. b) An image of the transparent electrotactile stimulator attached on pig skin. c) An illustration of the experimental setup for performing the electrical stimulation and recording test using the electrotactile stimulator; simulators are attached on both sides of the pig skin. d) The voltage measured from the recorders (2), (3), and (4) shown in (c). e) The recorded voltage as a function of the number of skin layers for different stimulation currents. f) Plot of the minimum required stimulation current for perception as a function of the frequency. g) FEA results of the three-dimensional electrical potential distributions of the skin in the case of direct stimulation using the electrotactile stimulator. h) The resistance of the serpentine GP electrode as a function of the applied strain. i) FEA results showing the strain distributions on the stimulator/recorder under the 30% stretching.

substrate. Finally, the electrotactile stimulator is transferred onto the skin by dissolving the PVA layer with water.[3]

Pig skin is used to characterize charge-injection properties of electrotactile stimulators. Electrotactile stimulators and recording electrodes are conformally placed on the top and bottom side of pig skin, respectively (Figure 5b). Figure 5c shows the experimental setup and the distance between stimulating and recording electrodes. The distance between electrodes considering the pig skin thickness is 0.3 cm (between (1) and (2)), 1.044 cm (between (1) and (3)), and 1.446 cm (between (1) and (4)). The voltage recorded from the electrode (2), (3), and (4) decreases as the distance from the electrode (1) increases (Figure 5d). When 5 mA is applied, the voltage measured at the electrode (3) and (4) decreases 24.2% and 32.7% from that measured at the electrode (2) due to the inversely proportional relationship between the potential and the distance under the constant electric field. For the same reason, the recorded voltage decreases as the skin thickness increases (Figure 5e; 39.6% and 48.7% voltage decrease with 200% and 300% skin thickness increase, under 5 mA). To provide perceptions using electrical stimulation, voltage greater than the threshold value of perception should be applied; this voltage varies with the thickness of the skin.[39] Figure 5f is a plot of the perception current as a function of the stimulation frequency, showing that the minimum perceptible current is inversely proportional to the frequency.[40] The reason why the minimum perceptible current is inversely proportional to the stimulation frequency is because of the more contribution of the skin capacitance component to the current flow at higher stimulation frequencies. The spatial distribution of the mechanoreceptors that could be successfully stimulated is estimated using FEA (Figure 5g, and see the Supporting Information for the details of FEA). Even after the stimulator is stretched by more than ~30%[4] (Figure S8), it shows the stable performance (Figure 5h) resulting in the effective charge injection. Figure 5i shows the distribution of the strain on the stimulator under stretching (see the Supporting Information for details of the strain distribution estimation).

The developed iHMI system is used to interactively control a robot arm (AX-18A, ROBOTIS, Korea). **Figure 6**a,b show the flow chart and the corresponding experimental setup for the iHMI demonstration, respectively. Motions such as the relaxing, bending, and pressing of a human wrist are detected by the piezoelectric motion sensor. Generated electrical signals are transmitted to a computer via a data acquisition (DAQ) board (NI USB-6289, National Instruments, USA). The DAQ processes the data using a specially written software program (LabVIEW, National Instruments, USA; Figure S9; see the Supporting Information for details of the program algorithm). The program analyzes signals acquired from sensors, distinguishes between different types of motions, and delivers appropriate commands to the robot arm. If the piezoelectric pressure sensor mounted on the gripper detects the object grasped by the robot arm, the stimulator laminated on the user's forearm

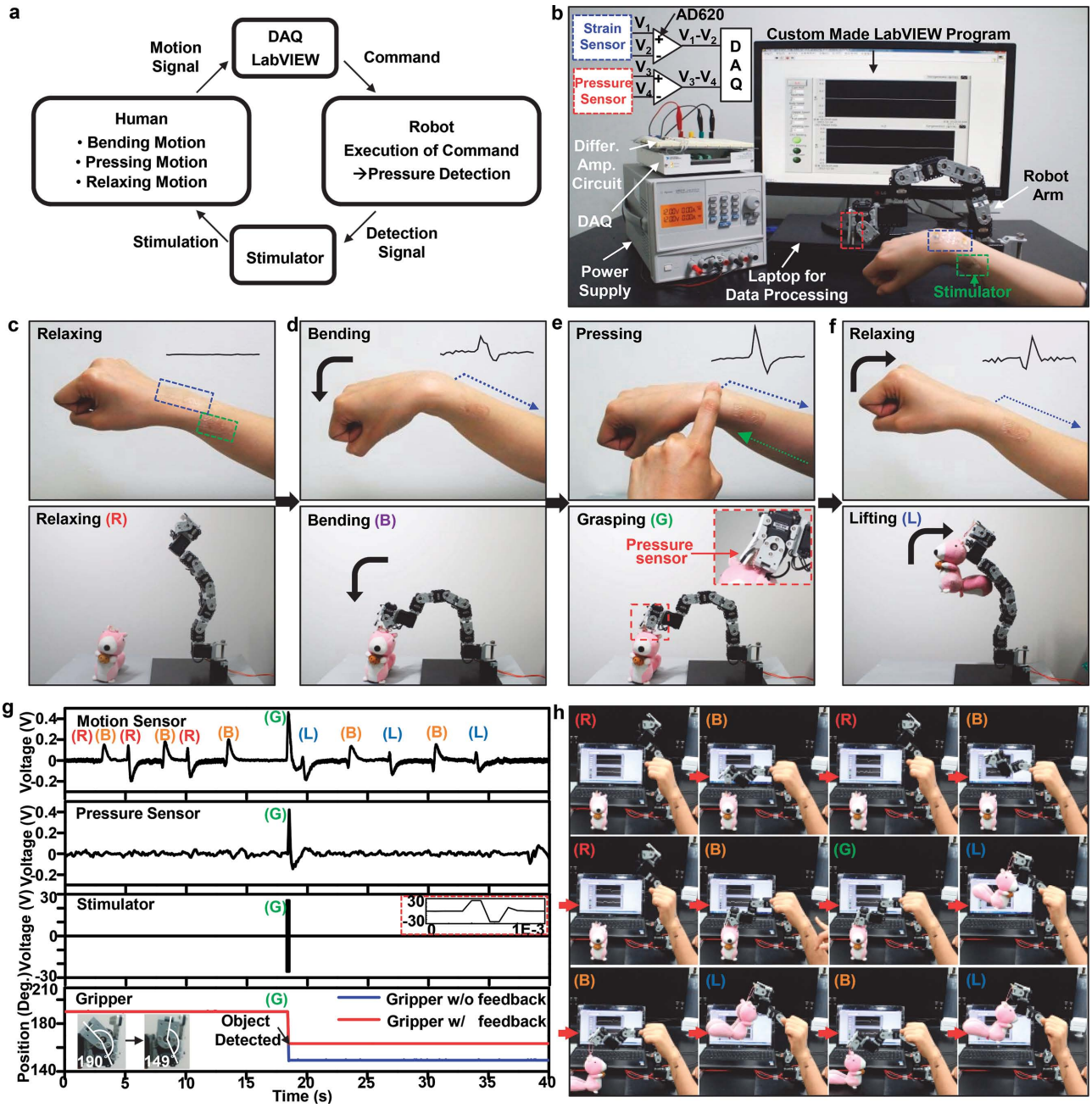

Figure 6. Use of the iHMI system, which consists of transparent devices (motion/pressure sensors and an electrotactile stimulator). a) A flow chart and b) the corresponding experimental setup for the iHMI demonstration. c) The transparent motion sensor (blue dotted box) and the electrotactile stimulator (green dotted box) are attached on the top side of the wrist and the lateral side of the forearm, respectively. The robot arm remains still if no motion is detected. d–f) The bending, pressing, and relaxing of the wrist cause the robot arm to bend, grasp, and lift, respectively. g) Detected signals acquired by the transparent motion sensor (first row) and by the pressure sensor on the gripper (second row), and the stimulation signal delivered by the transparent stimulator (third row). A magnified plot of the stimulation signal is shown in the inset of the graph on the third row. The measured positional statuses of the gripper without feedback control (blue) and with feedback control (red) during its closing motion are shown in the fourth row. The maximum movement of the gripper ranged from 149° (completely closed) to 190° (completely open, bottom left inset of the graph on the fourth row). h) Snapshots captured from the Movie S1, showing representative motions of the robot arm. The acronyms in g) and h) indicate specific motions in c–f) which uses the same acronyms.

applies a feedback electrical stimulation as an alert to the user. Differential operational amplifiers (AD620) with a unity gain are used to reduce the output impedance so that crosstalk can be prevented (Figure 6b, upper-left inset). The transparent motion sensor (Figure 6c, blue dotted box) and the electrotactile stimulator (Figure 6c, green dotted box) are attached on the top side of the wrist and the lateral side of the forearm, respectively. Bending, pressing, and relaxing motions of the wrist cause the

motion sensor to generate electrical signals with certain shapes (Figure 6c–f, upper-right inset); these are transmitted to the computer (Figure 6d–f, blue arrows). In response, pre-designated commands in the software cause the robot arm to exhibit bending, grasping, and lifting motions (Figure 6d–f, below).

Figure 6g shows representative data collected from the motion sensor (first row) and the pressure sensor (second row) on the wrist, the stimulator signal (third row), and the pressure sensor data on the gripper (fourth row). The position of the robot arm is recorded simultaneously during the demonstration (Figure S10). When the motion sensor is pressed (Figure 6g, first row, (G)), the amplitude of the generated peak is higher than that in the bending motion (Figure 6g, first row, (B)). If the amplitude is higher than a specific threshold, the program sends a command to the robot arm to grasp the target object. If an object is detected by the pressure sensor on the gripper (Figure 6g, second row, (G)), an electrotactile stimulation (Figure 6g, third row, (G)) is applied to the user and the gripper stops moving. This prevents the object from being pressed excessively (Figure 6g, fourth row, (G)). The stimulation signal is a high-frequency square wave (Figure 6g, third row, upper-right inset). Figure 6h shows snapshots from the video of the robot control demonstration (Movie S1, Supporting Information). The colorized acronyms in Figure 6c–g are the same as those in Figure 6h.

3. Conclusion

The transparent and stretchable piezoelectric motion/pressure sensors and electrotactile stimulators fabricated using GP heterostructures exhibit significant improvements over conventional rigid devices, when used as a wearable iHMI system. The transparent and skin-conforming characteristics make the wearable iHMI system invisible and give it a natural look. The ultrathin stretchable electrodes, which are constructed using serpentine GP heterostructures with embedded AgNWs networks, exhibit high conductivity and transparency. The SWNT-embedding PLA film shows an enhanced piezoelectricity than the conventional PLA. In combination, these functionalities, namely, the high transparency, stretchability and conductivity, the ultrathin and lightweight design, and the high SNR result in the current iHMI system shows unprecedented wearability and performance and allows for elaborate interactive robot control.

4. Experimental Section

A detailed description of fabrication procedures and characterization methods is available in the Supporting Information.

Fabrication of Transparent Wearable Motion/Pressure Sensor: A schematic description of the fabrication processes is shown in Figure S4 (Supporting Information). PLA (Sigma Aldrich, USA) is dispersed in a concentration of 3 wt% in chloroform (98.5%, Samchun, Korea) using a magnetic stirrer. SWNTs (Hanhwa, Korea) are also dispersed (1.6×10^{-6} wt%) in chloroform under sonication. The two dispersions then are drop cast on a slide glass to form the PLA/SWNTs composite. After the dispersions have been dried for 24 h at room temperature, the resulting PLA/SWNTs composite film (≈70 μm in thickness) is detached from the slide glass. Next, PMMA is spin coated on the synthesised GP sheet, and the backside of the GP sheet is exposed to Au doping solution (see the Supporting Information for the details of synthesis and doping process). The Au-doped GP/PMMA film is transferred onto the PLA/SWNTs composite film. Finally, another Au-doped GP/PMMA film is transferred onto the other side of the PLA/SWNTs composite film.

Fabrication of Transparent Wearable Electrotactile Stimulator: A schematic description of the fabrication processes is shown in Figure 5a. The fabrication starts with the metallization (Cr/Ni, 7 nm/70 nm thick) of a bare Si wafer and is followed by the spin coating of a negative epoxy resist (SU8, Microchem, USA) on the substrate. The epoxy pattern is defined through photolithography. Next, a layer of GP is transferred onto the substrate. Then, a dispersion of AgNWs is spin coated at 3000 rpm onto the GP layer for 30 s and baked at 200 °C for 5 min. Finally, a second layer of GP is transferred onto the GP layer with the embedded AgNWs and is isolated using reactive ion etching (O_2 plasma, 150 sccm, chamber pressure of 150 mTorr, radio frequency power of 100 W, etching time of 20 s). The top epoxy layer is patterned through photolithography. A layer of PMMA is spin coated on top; this layer serves as the support layer. A nickel etchant is used to remove the nickel film, which acts as the sacrificial layer. After the completion of the etching process, the stimulator is transferred onto the PDMS/PVA film. Finally, the PMMA layer on the device is removed with acetone.

Wiring Connection Methods of the Motion Sensors and Electrotactile Stimulator: Silver paste is used to connect flexible copper wire (diameter 150 μm, enamel encapsulated) to the gold pad of the motion sensor for transmitting the signal to the external DAQ board. After the silver paste had been cured completely, an epoxy (Araldite, Ciba-Geigy, Switzerland) is applied to the cured silver paste to ensure that the connection stayed stable during motion. In the case of the electrotactile stimulator, a flexible cable (i.e., an anisotropic conductive film (Elform, USA)) is used to connect the stimulator to the power supply. The film is subjected to a high enough temperature (160–180 °C) and pressure (2–3 MPa) to activate the adhesive of the film and ensure a robust connection.

Supporting Information

Supporting Information is available from the Wiley Online Library or from the author.

Acknowledgements

S.L., D.S., and J.K. contributed equally to this work. This work was supported by IBS-R006-D1. This work was also supported by a grant from the Basic Science Research Program of the National Research Foundation of Korea (NRF), funded by the Ministry of Science, ICT, and Future Planning (2012R1A1A1004925). This work was supported by the Seoul National University Research Grant.

Received: August 29, 2014
Revised: October 17, 2014
Published online: November 14, 2014

[1] S. Feng, R. Caire, B. Cortazar, M. Turan, A. Wong, A. Ozcan, *ACS Nano* **2014**, *8*, 3069.
[2] D. J. Wile, R. Ranawaya, Z. H. T. Kiss, *J. Neurosci. Methods* **2014**, *230*, 1.
[3] D.-H. Kim, N. Lu, R. Ma, Y.-S. Kim, R.-H. Kim, S. Wang, J. Wu, S. M. Won, H. Tao, A. Islam, K. J. Yu, T.-I. Kim, R. Chowdhury, M. Ying, L. Xu, M. Li, H.-J. Chung, H. Keum, M. McCormick, P. Liu, Y.-W. Zhang, F. G. Omenetto, Y. Huang, T. Coleman, J. A. Rogers, *Science* **2011**, *333*, 838.
[4] D. Son, J. Lee, S. Qiao, R. Ghaffari, J. Kim, J. E. Lee, C. Song, S. J. Kim, D. J. Lee, S. W. Jun, S. Yang, M. Park, J. Shin, K. Do,

M. Lee, K. Kang, C. S. Hwang, N. Lu, T. Hyeon, D.-H. Kim, *Nat. Nanotechnol.* **2014**, *9*, 397.
[5] J.-W. Jeong, W.-H. Yeo, A. Akhtar, J. J. S. Norton, Y.-J. Kwack, S. Li, S.-Y. Jung, Y. Su, W. Lee, J. Xia, H. Cheng, Y. Huang, W.-S. Choi, T. Bretl, J. A. Rogers, *Adv. Mater.* **2013**, *25*, 6839.
[6] R. H. Reuss, B. R. Chalamala, A. Moussessian, M. G. Kane, A. Kumar, D. C. Zhang, J. A. Rogers, M. Hatalis, D. Temple, G. Moddel, B. J. Eliasson, M. J. Estes, J. Kunze, E. Handy, E. S. Harmon, D. B. Salzman, J. M. Woodall, M. A. Alam, J. Murthy, S. C. Jacobsen, M. Olivier, D. Markus, P. M. Campbell, E. Snow, *Proc. IEEE* **2005**, *93*, 1239.
[7] R. C. Webb, A. P. Bonifas, A. Behnaz, Y. Zhang, K. J. Yu, H. Cheng, M. Shi, Z. Bian, Z. Liu, Y.-S. Kim, W.-H. Yeo, J. S. Park, J. Song, Y. Li, Y. Huang, A. M. Gorbach, J. A. Rogers, *Nat. Mater.* **2013**, *12*, 938.
[8] T. Someya, Y. Kato, T. Sekitani, S. Iba, Y. Noguchi, Y. Murase, H. Kawaguchi, T. Sakurai, *Proc. Natl. Acad. Sci. U.S.A.* **2005**, *102*, 12321.
[9] T. Sekitani, U. Zschieschang, H. Klauk, T. Someya, *Nat. Mater.* **2010**, *9*, 1015.
[10] K. Takei, T. Takahashi, J. C. Ho, H. Ko, A. G. Gillies, P. W. Leu, R. S. Fearing, A. Javey, *Nat. Mater.* **2010**, *9*, 821.
[11] C. Wang, D. Hwang, Z. Yu, K. Takei, J. Park, T. Chen, B. Ma, A. Javey, *Nat. Mater.* **2013**, *12*, 899.
[12] W. Yang, J. Chen, X. Wen, Q. Jung, J. Yang, Y. Su, G. Zhu, W. Wu, Z. L. Wang, *ACS Appl. Mater. Interfaces* **2014**, *6*, 7479.
[13] S. Wang, Y. Xie, S. Niu, L. Lin, Z. L. Wang, *Adv. Mater.* **2014**, *26*, 2818.
[14] S. C. B. Mannsfeld, B. C.-K. Tee, R. M. Stoltenberg, C. V. H.-H. Chen, S. Barman, B. V. O. Muir, A. N. Sokolov, C. Reese, Z. Bao, *Nat. Mater.* **2010**, *9*, 859.
[15] D. J. Lipomi, M. Vosgueritchian, B. C.-K. Tee, S. L. Hellstrom, J. A. Lee, C. H. Fox, Z. Bao, *Nat. Nanotechnol.* **2011**, *6*, 788.
[16] S. Jung, J. H. Kim, J. Kim, S. Choi, J. Lee, I. Park, T. Hyeon, D.-H. Kim, *Adv. Mater.* **2014**, *26*, 4825.
[17] S. Gong, W. Schwalb, Y. Wang, Y. Chen, Y. Tang, J. Si, B. Shirinzadeh, W. Cheng, *Nat. Commun.* **2014**, *5*, 3132.
[18] K. S. Kim, Y. Zhao, H. Jang, S. Y. Lee, J. M. Kim, K. S. Kim, J.-H. Ahn, P. Kim, J.-Y. Choi, B. H. Hong, *Nature* **2009**, *457*, 706.
[19] Z. Wu, Z. Chen, X. Du, J. M. Logan, J. Sippel, M. Nikolou, K. Kamaras, J. R. Reynolds, D. B. Tanner, A. F. Hebard, A. G. Rinzler, *Science* **2004**, *305*, 1273.
[20] L. Hu, H. S. Kim, J.-Y. Lee, P. Peumans, Y. Cui, *ACS Nano* **2010**, *4*, 2955.
[21] A. Morag, V. Ezersky, N. Froumin, D. Mogiliansky, R. Jelinek, *Chem. Commun.* **2013**, *49*, 8552.
[22] J. A. Rogers, M. G. Lagally, R. G. Nuzzo, *Nature* **2011**, *477*, 45.
[23] S. Xu, Y. Qin, C. Xu, Y. Wei, R. Yang, Z. L. Wang, *Nat. Nanotechnol.* **2010**, *5*, 366.
[24] W. Wu, X. Wen, Z. L. Wang, *Science* **2013**, *340*, 952.
[25] M. Lee, C.-Y. Chen, S. Wang, S. N. Cha, Y. J. Park, J. M. Kim, L.-J. Chou, Z. L. Wang, *Adv. Mater.* **2012**, *24*, 1759.
[26] L. Persano, C. Dagdeviren, Y. Su, Y. Zhang, S. Girardo, D. Pisignano, Y. Huang, J. A. Rogers, *Nat. Commun.* **2013**, *4*.
[27] T. Yoshida, K. Imoto, T. Nakai, R. Uwami, T. Kataoka, M. Inoue, T. Fukumoto, Y. Kamimura, A. Kato, Y. Tajitsu, *Jpn. J. Appl. Phys.* **2011**, *50*.
[28] Z. L. Wang, J. Song, *Science* **2006**, *312*, 242.
[29] Y. Qi, J. Kim, T. D. Nguyen, B. Lisko, P. K. Purohit, M. C. McAlpine, *Nano Lett.* **2011**, *11*, 1331.
[30] N. Lu, C. Lu, S. Yang, J. Rogers, *Adv. Funct. Mater.* **2012**, *22*, 4044.
[31] W.-H. Yeo, Y.-S. Kim, J. Lee, A. Ameen, L. Shi, M. Li, S. Wang, R. Ma, S. H. Jin, Z. Kang, Y. Huang, J. A. Rogers, *Adv. Mater.* **2013**, *25*, 2773.
[32] I. N. Kholmanov, C. W. Magnuson, A. E. Aliev, H. F. Li, B. Zhang, J. W. Suk, L. L. Zhang, E. Peng, S. H. Mousavi, A. B. Khanikaev, R. Piner, G. Shvets, R. S. Ruoff, *Nano Lett.* **2012**, *12*, 5679.
[33] Y. Hao, M. S. Bharathi, L. Wang, Y. Liu, H. Chen, S. Nie, X. Wang, H. Chou, C. Tan, B. Fallahazad, H. Ramanarayan, C. W. Magnuson, E. Tutuc, B. I. Yakobson, K. F. McCarty, Y.-W. Zhang, P. Kim, J. Hone, L. Colombo, R. S. Ruoff, *Science* **2013**, *342*, 720.
[34] C. Peng, Z. Jia, D. Bianculli, T. Li, J. Lou, *J. Appl. Phys.* **2011**, *109*.
[35] M.-S. Lee, K. Lee, S.-Y. Kim, H. Lee, J. Park, K.-H. Choi, H.-K. Kim, D.-G. Kim, D.-Y. Lee, S. Nam, J.-U. Park, *Nano Lett.* **2013**, *13*, 2814.
[36] K. I. Park, J. H. Son, G.-T. Hwang, C. K. Jeong, J. Ryu, M. Koo, I. Choi, S. H. Lee, M. Byun, Z. L. Wang, K. J. Lee, *Adv. Mater.* **2014**, *26*, 2514.
[37] K.-I. Park, S. Xu, Y. Liu, G.-T. Hwang, S.-J. L. Kang, Z. L. Wang, K. J. Lee, *Nano Lett.* **2010**, *10*, 4939.
[38] S. Xu, Y. Yeh, G. Poirier, M. C. McAlpine, R. A. Register. *Nan. Yao, Nano Lett.* **2013**, *13*, 2393.
[39] P. Delmas, J. Hao, L. Rodat-Despoix, *Nat. Rev. Neurosci.* **2011**, *12*, 139.
[40] M. Ying, A. P. Bonifas, N. Lu, Y. Su, R. Li, H. Cheng, A. Ameen, Y. Huang, J. A. Rogers, *Nanotechnology* **2012**, *23*.